Official journal of the JHL 2689-9620
www.light-am.com

Review Open Access

Review of laser powder bed fusion (LPBF) fabricated Ti-6Al-4V: process, post-process treatment, microstructure, and property

Sheng Cao[1,*], Yichao Zou[1], Chao Voon Samuel Lim[2,3] and Xinhua Wu[2,3]

Abstract

Laser powder bed fusion (LPBF) is a timely important additive manufacturing technique that offers many opportunities for fabricating three-dimensional complex shaped components at a high resolution with short lead times. This technique has been extensively employed in manufacturing Ti-6Al-4V parts for aerospace and biomedical applications. However, many challenges, including poor surface quality, porosity, anisotropy in microstructure and property, and difficulty in tailoring microstructure, still exist. In this paper, we review the recent progress in post-process treatment and its influence on the microstructure evolution and material performance, including tensile, fatigue, fracture toughness, creep, and corrosion properties. The contradictions in simultaneously achieving high strength/ductility and strength/fracture toughness/creep resistance have been identified. Furthermore, research gaps in understanding the effects of the emerging bi-modal microstructure on fatigue properties and fracture toughness require further investigation.

Introduction

Ti-6Al-4V, also termed as TC4, titanium grade 5 and grade 23 (extra low interstitials), is the most commonly used Ti alloy[1,2]. It combines excellent properties including good mechanical performance, outstanding corrosion resistance, and superior biocompatibility. Therefore, Ti-6Al-4V is widely applied in aerospace, automotive, marine and chemical industries. Furthermore, it has been widely used in biomechanical applications such as implants and prostheses[1–3]. The details of the Ti-6Al-4V powders are available in the ASTM and AMS specifications[4,5].

Ti-6Al-4V is an α+β titanium alloy with a hexagonal close packed (HCP) α phase stable at low temperatures, and a body centered cubic (BCC) β phase stable at high temperatures[1]. The β/α allotropic transformation temperature (β transus) is approximately 995 °C for Ti-6Al-4V[2], and this temperature can be increased by adding α stabilizers (Al, O, N, and C) and decreased by alloying with β stabilizers (V, Mo, Fe, etc.)[1,2]. The crystal structures of α and β phases are shown in Fig. 1. Similar to another HCP/BCC metal Zr[6], the crystallographic orientation relationship between HCP Ti (α) and BCC Ti (β) obeys the Burgers orientation relationship for which $\{0001\}_\alpha//\{110\}_\beta$ and $<11\bar{2}0>_\alpha//<111>_\beta$[1].

In Al-containing Ti alloys, the precipitation of ordered and coherent Ti_3Al (α_2) phase can occur in α grains after ageing at low temperatures of approximately 500 °C when the Al content is at 6 wt.%[7–9]. Specifically, α_2 has a hexagonal $D0_{19}$ superlattice structure[1], in which the lattice parameter on the basal plane is twice that of α phase, whereas the lattice parameter remains the same on the *c*-

Correspondence: Sheng Cao (sheng.cao@yahoo.com)
[1]Department of Materials, The University of Manchester, Oxford Road, Manchester, M13 9PL, UK
[2]Monash Centre for Additive Manufacturing, Monash University, VIC 3800, Australia
Full list of author information is available at the end of the article.

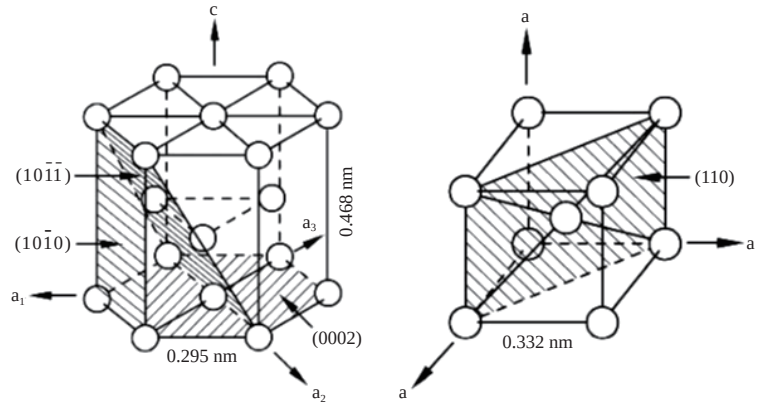

Fig. 1 Crystal structures of HCP α and BCC β phases in titanium[1].

axis. The α_2 solvus temperature is approximately 550 °C for Ti-6Al-4V[1]. Similar to the influence on β transus, Al and O are α_2 stabilizers, which extend $\alpha+\alpha_2$ phase field to higher temperatures and promote the ordering transformation. Ordered α_2 phase introduces precipitation hardening, and it is an extremely brittle intermetallic phase[1,2]. The presence of α_2 results in non-homogeneous planar slip, and increases the effective slip length and strain localization[10,11], which has detrimental effects on microcrack propagation, low cycle fatigue (LCF) resistance, and stress corrosion cracking resistance[1,12].

Rapid cooling from temperatures above the martensitic start temperature (M_s) leads to diffusionless transformation. The martensite start temperature (M_s) in Ti-6Al-4V has been reported in a wide temperature range from 575 °C to 800 °C[13–15], and a lower M_s has been observed at a higher cooling rate[15]. Similar to β transus and α_2 solvus temperatures, the martensitic start temperature is affected by the alloying elements. In general, the metastable martensite is hexagonal α' in Ti-6Al-4V, and the Burgers orientation relationship is still valid between β and α'[1]. Given that the interstitial O atoms only introduce a small elastic distortion in α' martensite, the martensitic hardening leads to a slight increase in strength. Orthorhombic α'' martensite is rarely observed in the low V containing Ti-6Al-4V. The martensite type can be determined by the temperatures from which Ti-6Al-4V is quenched and the concentration of β stabilizers in the β phase at that temperature[3]. In the α+β phase field, the V concentration in β is dependent on the temperature. The formation of α'' is observed under conditions with a V concentration exceeding 9 wt.%[1,3]. For example, the β phase is enriched with V concentration of up to 10 wt.% at a temperature range of 800−850 °C, and water quenching (WQ) from this temperature range leads to α'' martensite transformation[16]. In contrast to the hardening effect of HCP α' martensite, the orthorhombic α'' martensite is soft and can provide deformability[2,3]. Both metastable α' and α'' martensite phases can decompose into equilibrium α and β phases at suitable heat treatment temperatures.

The high cost of conventionally processed Ti alloys limits their applications, and crucial contributors to the expense are the significant material wastage, high energy input, and long lead times in conventional processing techniques[17]. Laser powder bed fusion (LPBF), as an advanced additive manufacturing (AM) technology, has attracted significant attention and has been implemented in research and industry over the last two decades. It has a wide range of advantages such as producing nearly fully dense and complex shaped components at a high resolution (which cannot be realized via conventional methods), high material utilization with limited machining, and reduced lead times[18,19].

Specifically, LPBF is a complicated metallurgical process, which involves powder melting and extremely fast directional solidification, re-melting and re-solidification during the subsequent scan tracks and layers, and post-solidification thermal cycling. The understanding of microstructure evolution during the LPBF process and post-process treatment is essential to obtain Ti-6Al-4V components with high quality and satisfied properties. In this review, the LPBF technique and its processing parameters are briefly introduced. Then, the possible types of defects, residual stress, and LPBF built surface are reviewed. Subsequently, the unique as-fabricated microstructure and microstructure evolution during the post-process treatment are summarized, and its effects on tensile, fatigue, fracture toughness, and creep properties are discussed.

Laser powder bed fusion

LPBF, also known as selective laser melting (SLM) or

direct metal laser melting (DMLM), was developed in the Fraunhofer Institute ILT in 1995[20]. It employs a focused laser beam to melt metallic powders within a selected area based on the cross-sectional slice of a 3-dimensional (3D) CAD model, and the melt pool is then solidified at a high cooling rate. After a layer has been scanned, the build platform is lowered by a depth, which is defined as the layer thickness. A new layer of powder is spread by the re-coater and melted by the focused laser beam based on the next cross-sectional slice. The layer-by-layer deposition is repeated in a protective atmosphere until all the slices of the CAD profiles are complete. Fig. 2 illustrates a typical LPBF system, which includes a processing laser, an automatic powder feed and overflow system, and an inert gas protection system[21,22]. After fabrication, unused powders can be collected from the overflow and powder bed. These collected powders can then be recycled and reused[23,24].

In-process parameter and defect

The main in-process parameters include laser power, laser spot size, scanning speed, hatch distance, layer thickness, and build platform pre-heating temperature. Among them, the most widely manipulated parameters are laser power and scan speed. Fig. 3a presents a processing window between these two parameters. A high laser powder and a low scan speed can introduce an excessive energy input, which can lead to liquid melt overheating, evaporation within the melt pool, and keyhole defects[25]. Conversely, a low laser power and a high scan speed can lead to insufficient energy density, which causes incomplete melting, inadequate penetration and lack-of-fusion defects[24,26,27]. In addition to laser power and scan speed, inappropriate hatch distance and layer thickness can also result in lack-of-fusion defects. Furthermore, balling can occur at high laser power and scan speeds even for a suitable energy density as shown in the top right corner of Fig. 3a[28,29]. Given that the increased laser power leads to a higher boosting effect on the maximum temperature achieved in the melt pool than the reverse effect from the increased scan speed[30,31], a higher peak melt pool temperature induces a more intense Marangoni flow, which can cause the Plateau-Rayleigh instability and balling[30,32,36]. An example of different types of defects in LPBF fabricated Ti-6Al-4V is illustrated in Fig. 3b–d. For an intermediate laser power of 175 W, gradually decreasing scan speeds are located in the three different regions of incomplete melting, processing window, and overheating as shown in Fig. 3a. Additionally, another type of defect is gas porosity, which is typically small in size[33]. The formation of gas pores can be related to two main causes: (a) the inert gas pores trapped within the powder feedstock during the powder atomization process are transferred to the part[34], and (b) after solidification, the protective gas can be trapped in the melt pool as bubbles due to the rapid cooling in LPBF fabrication[35].

In-situ thermal cycling

LPBF exhibits a unique thermal history including directional melting-solidifying against the heat transfer direction, subsequent re-melting/re-solidifying due to the following laser scan and deposited layer, and post-

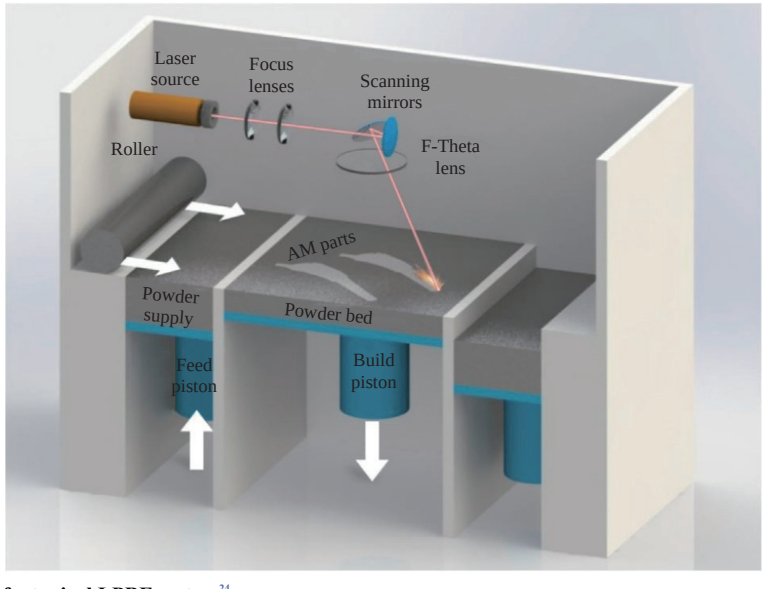

Fig. 2 Schematic diagram of a typical LPBF system[24].

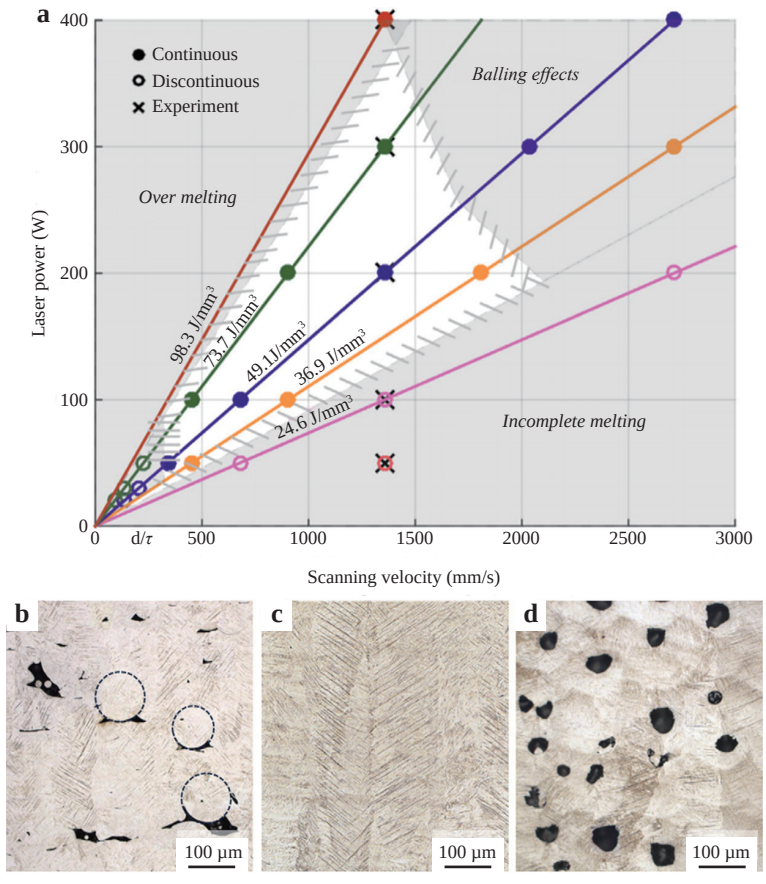

Fig. 3 A process window and various types of defects in LPBF fabricated Ti-6Al-4V. a A processing window for LPBF fabricated Ti-6Al-4V[28]. **b–d** The influence of scan speed on porosity types in LPBF fabricated Ti-6Al-4V with a fixed laser power of 175 W and a hatch distance of 100 μm[36]. **b** Lack-of-fusion due to insufficient penetration at a high scan speed. **c** A nearly fully dense microstructure density at an intermediate scan speed. **d** Keyhole type defects due to overheating at a low scan speed.

solidification cyclic heating/cooling[37–39]. Fig. 4 is a simulated thermal history of a given location in a LPBF fabricated Ti-6Al-4V[40], and there are thermal cycles from different laser scan vectors within a layer and thermal cycles in the following layers. After solidification from the peak temperature in layer P1, the material undergoes a series of thermal cycles in the following laser scan tracks and layers. When the next track is scanned or the next layer is deposited, the previously fabricated material can be partially re-melted and re-solidified. The combined effect of high laser power, fast laser scan speed, and small laser spot size leads to an extremely high heating and cooling rate[41–44]. According to an in-situ synchrotron experiment on LPBF fabricated Ti-6Al-4V, the maximum heating and cooling rates can reach the orders of 10^6 °C/s and 10^5 °C/s, respectively[45].

Residual stress

During LPBF fabrication, the high cooling rate and large thermal gradients lead to high levels of residual stress[46]. This can cause distortion and delamination, which results in parts failure and unacceptable dimensional change[47,48]. In general, residual stress varies with the build height. Fig. 5 shows the residual stress distribution in Ti-6Al-4V cuboids fabricated on large and small substrates measured by the contour method. Specifically, the tensile residual stress presents at the bottom of the substrate and top surface of the built sample with a large compressive stress region located in between according to simulations[49] and experimental contour method[50]. In the horizontal cross-section, high tensile residual stress/strain is generally located at the part edge, while compressive residual stress is at the part center[51]. More specifically, the tensile residual stress can exceed 900 MPa at the part edge[51], which is close to the yield strength of Ti-6Al-4V.

Tensile residual stress is deleterious to fatigue properties, because it tends to facilitate fatigue crack propagation[3]. In addition to the influence on fatigue, the

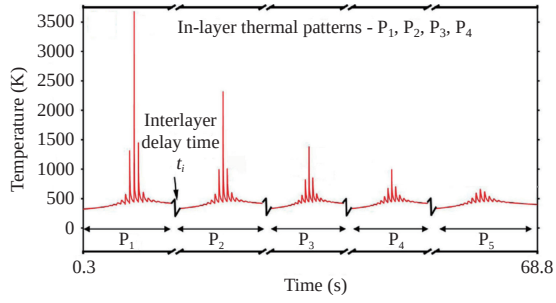

Fig. 4 Simulated thermal cycling history of a specific location in LPBF fabricated Ti-6Al-4V. This includes intralayer and interlayer reheating and cooling. P1 to P5 are different layers[40].

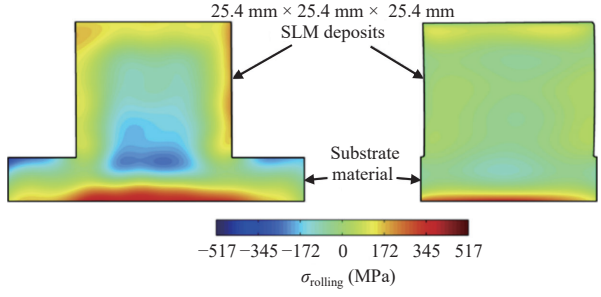

Fig. 5 Residual stress of LPBF fabricated Ti-6Al-4V measured via contour-method in the rolling direction of the substrate. Specimens are built on a large substrate with an overhang (left) and a small substrate without an overhang (right)[50].

parts removal from substrate without stress-relieving heat treatment would introduce deformation through strain/stress relaxation[46,49]. Therefore, efforts have been made to reduce the residual stress, including substrate heating during the LPBF process and post-process stress-relieving heat treatment. Furthermore, residual stress can be influenced by the in-process laser scan strategy and scan rotation between neighboring layers. A lower residuals stress was observed in the bi-directional scan than that resulting from a chessboard scan. Additionally, a scan rotation of 90° led to a reduced residual stress when compared with that in a scan rotation of 67°[52].

Surface roughness

The surface roughness can be controlled by the powder particle morphology and size, layer thickness, processing parameters, scan strategies, and the orientation relationship between the inclined surface and laser incident direction[53–58]. In addition, the frequently used support structures adversely affect the surface finish of LPBF fabricated parts even after support removal[59].

The surface of LPBF fabricated parts is covered by partially melted powder particles[57]. Hence, the powder characteristics affect the surface roughness. Given that LPBF is a layer-wise manufacturing process, a larger layer thickness leads to a rougher inclined surface owing to the staircase effect[53,54,58]. More importantly, laser processing parameters can influence the melt pool morphology[30], which in turn affects the surface quality. A few studies employed contour scans to improve the quality of the as-fabricated surface[56,58]. Other factors, including the location of the part on the substrate, the orientation relationship between the inclined surface and the laser incident direction, have also been found to influence the surface roughness[56].

Surface treatments after LPBF fabrication are generally applied to improve surface quality. The most commonly used treatments include blasting[57], shot peening[60], vibratory grinding/tribo-finishing[57,60], machining/micro-machining[18,57], and electropolishing[60]. The loosely attached powder particles on the surface of LPBF fabricated parts can be addressed by blasting and shot peening; however, the blasting and/or peening media can introduce deformations on the surface[57]; hence, they can only slightly reduce the surface roughness. In addition, shot peening results in work hardening and compressive residual stress in the surface layer, which prevent the fatigue crack initiation from the surface[61]. Vibratory grinding leads to a smoother surface, and it provides a better surface finish (R_a) of a few μm when compared with blasting and shot peening. Machining and electropolishing are effective methods to remove the surface layer, which contributes to the lowest surface finish (R_a) below 1 μm[57,60].

Process and microstructure

As-fabricated microstructure

Typical LPBF microstructure

The directional solidification, rapid cooling after melting, and subsequent thermal cycling result in a non-equilibrium hierarchical as-fabricated microstructure of epitaxial grown prior-β grains aligned in the opposite direction of the cooling direction, and these columnar β grains consist of a few sets of fine acicular α' martensite variants[16,31,38,62–67]. The processing parameters affect the as-fabricated microstructure. A recent study showed that a higher laser energy density leads to a larger prior-β grain width and a smaller α' martensite size[68]. In addition to the columnar grains, the partial re-melting of the previously solidified layers leads to a strong β solidification texture. As shown in Fig. 6, a preferred $\{100\}_\beta$ texture along the grain growth direction has been found on the BCC orientation map reconstructed from electron back-scatter diffraction (EBSD) data of HCP Ti (α and/or α') based on

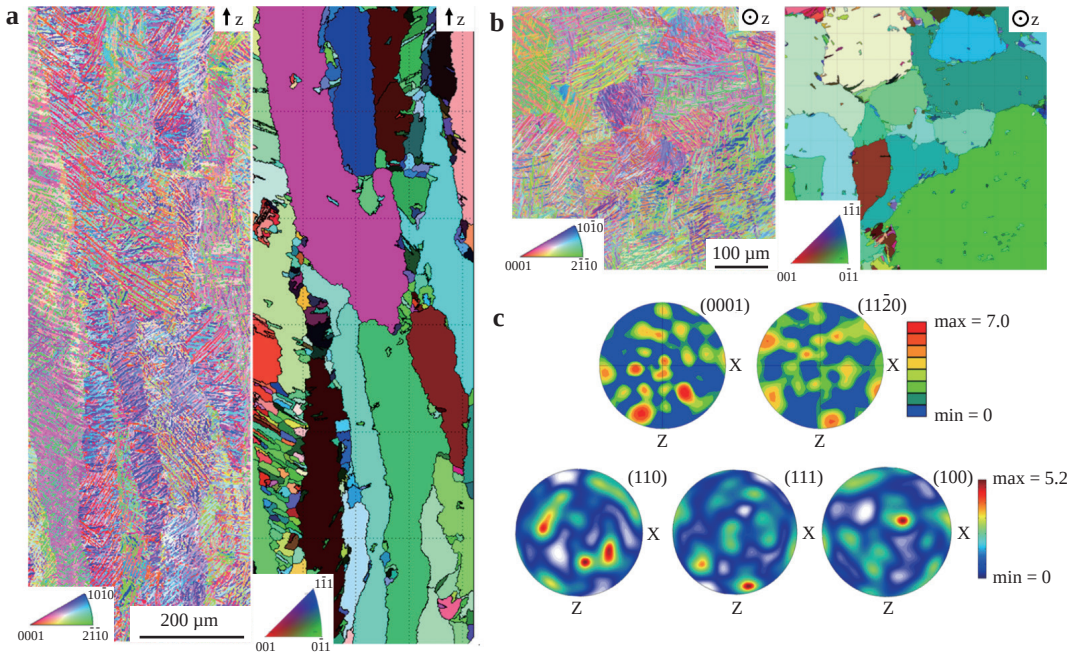

Fig. 6 Grain orientations and textures of LPBF fabricated Ti-6Al-4V. a Orientation maps of HCP Ti and reconstructed BCC Ti taken from a vertical plane[62]. **b** Orientation maps of HCP Ti and reconstructed BCC Ti taken from a horizontal plane[63]. **c** The corresponding pole figures of HCP Ti and reconstructed BCC Ti of the vertical plane in a[62].

the Burgers orientation relationship[62,63]. It is important to note that the β grain growth direction can be influenced by the thermal flux direction, which is affected by the laser scan speed and strategy[38,62]. As a result, the growth direction of β grain can be either parallel or inclined at a certain angle to the macroscopic build direction (Z)[31,62]. The pole figure in Fig. 6c is an example where the $\{100\}_\beta$ texture in the grain growth direction is inclined approximately 20° away from the build direction[62].

A few studies have shown that a small amount of β can be detected by synchrotron XRD[69], EBSD[70], and TEM[71] in specimens fabricated at either high laser powers or short hatch distances. Fig. 7a shows an α+β microstructure at the middle height of a sample manufactured with a short hatch distance[71]. Both high laser power and short hatch distance can increase the in-process temperatures achieved and the time at high temperatures during the intrinsic thermal cycling[45]. These factors facilitate the deposition of metastable martensite into α+β phases. In addition to β, a few studies have reported α_2 precipitates in the as-fabricated sample based on TEM and synchrotron XRD results[38,71]. Fig. 7b shows the superlattice reflection of α_2 formed in α lamella, and the formation of α_2 is believed to be related to the thermal cycling at temperatures just below the α_2 solvus. Carefully controlled Al and O compositions in the Ti-6Al-4V powders and the low O concentration in the printing atmosphere can suppress the α_2 precipitation.

In general, the as-fabricated Ti-6Al-4V has a fully α' martensitic microstructure. As a result of thermal cycles, α' martensite has a hierarchical structure with different width and length, which can be identified as primary, secondary, tertiary and quartic α', and their formation mechanism has been described in detail in a recent study[72]. Within the α' martensite, lattice defects, including dislocations, stacking faults and twins, are present[73,74]. A high density of dislocations has been identified in α' plate via TEM[69] and diffraction peak broadening phenomenon in high energy XRD[70]. The TEM dislocation analysis ($g \cdot b$ test) revealed the presence of both <*a*> and <*c*+*a*> dislocations within martensite, which indicates that significant plastic deformation occurs during the LPBF process[69].

In principle, $\{10\bar{1}1\}\langle 10\bar{1}2\rangle$ and $\{11\bar{2}2\}\langle 11\bar{2}3\rangle$ twins can be activated when compression is applied along the *c*-axis, while $\{10\bar{1}2\}\langle 10\bar{1}\bar{1}\rangle$ and $\{11\bar{2}1\}\langle 11\bar{2}\bar{6}\rangle$ twins can occur when tension is applied along the *c*-axis for HCP titanium[75]. In LPBF fabricated Ti-6Al-4V, compression $\{10\bar{1}1\}$[76,77] and $\{11\bar{2}2\}$ twins[69], and tension $\{10\bar{1}2\}$[69,72,78,79] twins have been reported in hexagonal α' martensite as shown in Fig. 8. A previous work has suggested that tension $\{10\bar{1}2\}$ twins can accommodate the tensile residual stress at the top region of LPBF fabricated parts[79], but this does not explain the co-existing compression and tension twins in the same TEM sample. Some studies have shown that twinning is related to the martensitic transformation of

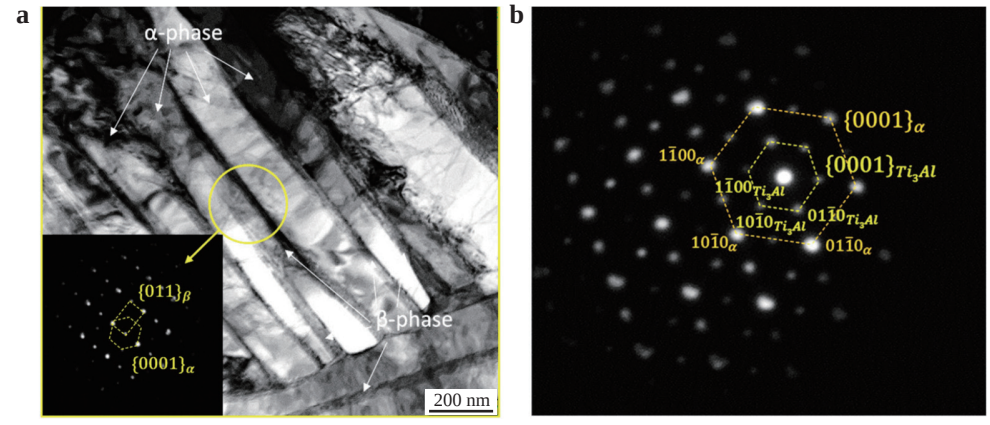

Fig. 7 β and α_2 phases detected in the as-fabricated LPBF Ti-6Al-4V. a TEM bright field image showing an α+β microstructure in the middle height (Z~ 5 mm) of a Ti-6Al-4V sample[71]. **b** Selected Area Diffraction (SAD) pattern of ordered α_2 within an α plate[71].

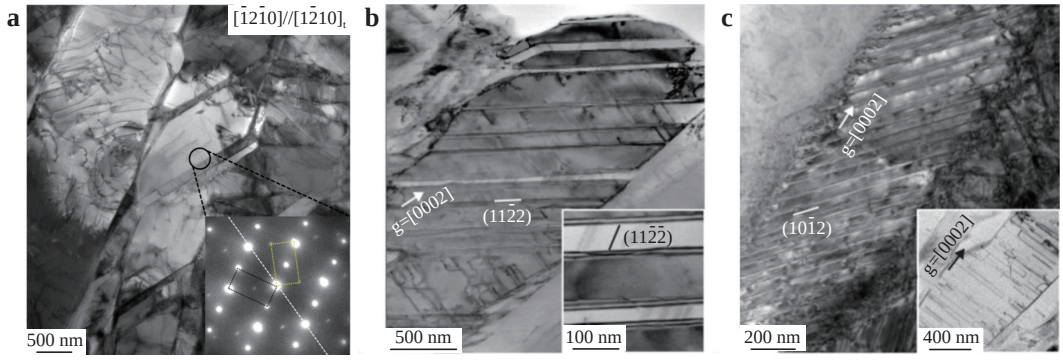

Fig. 8 Lattice defects of twins and dislocations in LPBF fabricated Ti-6Al-4V. a $\{10\bar{1}1\}<10\bar{1}2>$ type twin[76]. **b** $\{11\bar{2}2\}<11\bar{2}3>$ type twin[69]. **c** $\{10\bar{1}2\}<10\bar{1}\bar{1}>$ type twin[69].

β→α'[76,80]. However, this can only explain the activation of $\{10\bar{1}1\}$ twins. A recent study has proposed that thermal cycles of fast heating to and rapid cooling from different peak temperatures and associated solid state phase transformation can lead to the formation of both compression and tension twins in LPBF fabricated Ti-6Al-4V[81].

In addition to hexagonal α' martensite, orthorhombic martensite α'' has been reported in as-fabricated Ti-6Al-4V in a few studies[66,77,78]. For samples fabricated at the same LPBF parameters, α'' was observed in one of the Ti-6Al-4V cuboids with a larger horizontal (X-Y) cross section area. The results suggested that faster cooling related to the larger heat conduction area on the horizontal cross section could lead to α'' formation[77]. However, the discussion is missing regarding the influence of horizontal cross-sectional area on the temperature achieved during the post-solidification thermal cycling. During LPBF, thermal cycling can heat some previously deposited layers to intermediate temperatures in the α+β phase field. At these temperatures, element segregation occurs and β phase is enriched in V. Thus, rapid cooling from such temperatures would result in the formation of α'' martensite[78].

When compared to thermo-mechanically processed Ti-6Al-4V, as-fabricated LPBF Ti-6Al-4V exhibits higher strength but lower ductility due to the non-equilibrium α' martensitic microstructure[64,65,72,82] and residual stress built up during the LPBF process[83,84]. As a result, in-process measures and post-process treatments have been explored to promote the metastable martensite decomposition to equilibrium α+β phases and to minimize residual stress.

Preheated substrate and in-process heat treatment

During the LPBF process, a preheated substrate generally reduces the temperature gradients within the parts and decreases residual stress[85]. Substrates preheated to 370 °C and 570 °C can effectively reduce the residue stress by 71% and almost 100%, respectively, when compared to the sample built on a substrate heated to 100 °C[86]. For

LPBF fabricated α' martensite, TEM and in-situ XRD investigations revealed that martensite decomposition commences at a low temperature at 400 °C[87]. β phase has been observed in the as-deposited Ti-6Al-4V fabricated on a preheated substrate at 200 °C and with a tight hatch distance of 40 μm[71]. A substrate preheated at 500 °C results in a partially decomposed α' martensite microstructure[16], which improves elongation to approximately 10%[86]. However, high temperature preheating is not energy efficient, and can account for 40% of the total energy consumed in LPBF fabrication[88]. In addition, in a recent study, it was indicated that a preheated substrate at 550 °C leads to significant oxidation[89], because titanium suffers a high chemical affinity to oxygen at high temperatures. High oxygen content contributes two consequences, namely increased brittleness and deteriorated powder recyclability[90,91].

Other in-process measures, including manipulation of laser beam focal offset distance (FOD) and interlayer time, were used to increase the temperature achieved during the intrinsic thermal cycling and to promote the α' martensitic decomposition[92]. Specifically, FOD can control the laser spot diameter and the local applied energy within the laser beam[93], and an increased FOD generally leads to a decreased temperature and a shortened time window for in-situ martensite decomposition during the intrinsic thermal cycling[94]. Given that LPBF is a layer-by-layer deposition process, a short interlayer time of less than 12 s have been found to be effective in promoting the in-process martensite decomposition, which leads to a coarser α+β lamellar microstructure[95,96]. With a suitable FOD of 2 mm, an ultrafine fine α+β lamellar microstructure has been achieved in the as-deposited Ti-6Al-4V fabricated on support structures with a substrate preheated at 200 °C[64]. In addition to the FOD manipulation, all the aforementioned investigations included lattice support structures to decrease the amount of heat transferred to the substrate, thereby increasing the in-situ thermal cycling temperature. Support structures are known to introduce surface roughness even after support removal[59], which affect the as-built surface quality and its application in the as-built condition.

Post-process treatment

Stress-relieving

In general, stress-relieving treatments are carried out in the temperatures between 450 °C and 650 °C followed by air cool (AC) or furnace cool (FC) prior to the electrical discharge machining (EDM)[3,97]. For instance, a 2−4 h stress-relieving treatment at 595 °C followed by AC is recommended for Ti-6Al-4V weldment[3]. Such a heat treatment is generally performed in a protective argon atmosphere, which reduces oxidation and the formation of α case. As shown in Fig. 9, the time required for stress relief is dependent on temperature. A higher stress-relieving temperature decreases the required heat treatment time. For example, 1 h at 595 °C is equivalent to 5 h at 540 °C in terms of stress relief effectiveness[3]. As the stress-relieving temperature is relatively low in the α+β field, the as-deposited microstructure will be slightly coarsened although the size and variants of primary and secondary α/α' laths are maintained[98].

It should be noted that the α_2 solvus temperature is approximately 550 °C for Ti-6Al-4V[1], and it can be influenced by the Al and O content. A stress-relieving temperature below the α_2 solvus can lead to the precipitation hardening of α phase by α_2 particles[73], which is dependent on the Al and O concentration in the α phase. If the LPBF fabricated parts are used after stress relief, the stress-relieving temperature should be cautiously determined by whether α_2 formation is ideal for the application.

Annealing

It is widely accepted that the α' martensite formed in LPBF is brittle and responsible for the low elongation below 10% in the as-fabricated Ti-6Al-4V[31,64,70,78,83,84,96]. Such a low ductility does not satisfy the elongation requirement of 10% as per the specification of AM fabricated Ti-6Al-4V in ASTM 2 924–14[4]. Therefore, investigations have been focused on promoting the non-equilibrium α' martensite decomposition in the as-fabricated microstructure to an equilibrium α+β microstructure through annealing. Previous studies have revealed that annealing in the range of 750-900 °C can effectively facilitate the α' martensite decomposition and improve the ductility[76,99,100].

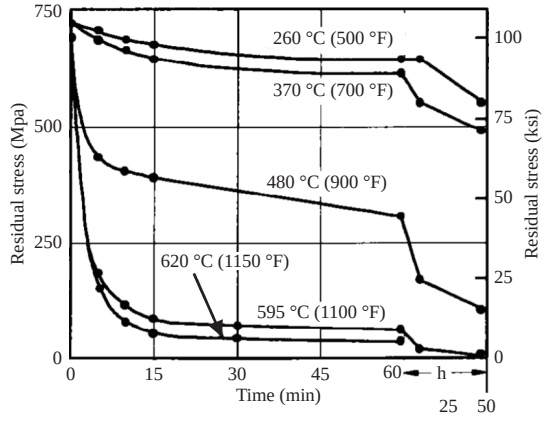

Fig. 9 Effect of stress-relieving temperatures on residual stress in Ti-6Al-4V[3].

When compared with the stress-relieving heat treatments, annealing is generally performed at relatively higher temperatures in the α+β phase field and followed by AC or FC[97]. A direct annealing can promote martensite decomposition into α and β phases, and the lamellar microstructure will be significantly coarser than the as-fabricated microstructure. A recent study has explicitly investigated the static coarsening behavior of lamellar structures in LPBF fabricated Ti-6Al-4V, which suggests that heat treatment temperatures at 900 °C or higher significantly accelerate the coarsening kinetics[101].

Solution treating and aging

In thermomechanically processed titanium alloys, solution treating and aging (STA) treatments are generally used to improve strength. Such a heat treatment has also been employed as a post-process treatment for LPBF fabricated Ti-6Al-4V, which can be categorized into β STA and α+β STA based on the solution temperature. As shown in Fig. 10, the β STA microstructure has significantly coarsened prior-β grains when heat treated at temperatures above the β transus, and β grains lose the columnar morphology on vertical plane[84,102]. Because all the α'/α lamellae transform to β phase solid solution at such temperatures, and β grains begin to grow[84]. For example, a β solution treatment at 1 015 °C for 2 h led to an increase in β grain width with unchanged length[84], and a heat treatment of 2 h at 1 050 °C resulted in equiaxed prior β grains in LPBF fabricated Ti-6Al-4V[102]. The width of α lamellae is related to the cooling rate after β solution treatment. After the β STA, there are fewer α variants left. This results in increased α colony size, which leads to a longer effective slip length for dislocations.

When compared to β STA, α+β STA is versatile in terms of achieving different microstructures, in which the size, volume fraction, and morphology of various phases can be manipulated. A 2 h α+β solution treatment followed by a slow cooling method, such as FC, generally leads to an α+β lamellar microstructure, and a small amount of equiaxed α can form at solution temperatures close to β transus[102,103]. If fast cooling methods such as AC or WQ are used, some β phases can transform to fine α_s (secondary α) or martensitic microstructure during cooling. Several studies have indicated that a bi-modal microstructure can be obtained in LPBF fabricated Ti-6Al-4V through post-process α+β STA treatments[102,104,105]. In addition to LPBF, the bi-modal microstructure has been reported in similar post-process sub-transus STA treated Ti-6Al-4V fabricated by other AM techniques including electron beam melting (EBM)[106], direct laser deposition (DLD)[107], and wire arc additive manufacturing (WAAM)[108].

As show in Fig. 11a, the microstructure is still mainly α+β lamellae for low to intermediate solution temperatures of up to 920 °C for 2 h followed by AC. This is due to the low equilibrium volume fraction of β phase when the solution temperature is exceedingly below the β transus, and the relatively slow AC used after solution treatment. Fig. 11b–d show that increases in solution temperatures lead to an increased β_t (transformed β) region, in which fine α_s precipitates are formed. In the meantime, the volume fraction of α_p (primary α) decreases, and the aspect ratio of α_p decreases with the formation of some equiaxed α_p grains. Fig. 11 also presents the influence of solution time, and a longer solution time results in a reduced number density of α_p, a larger sized α_p and a more globular α_p morphology.

In general, plastic deformation prior to heat treatment is essential for inducing globularization in thermomechanically processed Ti-6Al-4V. While in LPBF fabricated Ti-6Al-4V, plastic deformation is not required for the globularization to occur. Because the high dislocation density inherited from the LPBF process can initiate the globularization. The globularization mechanism is similar for LPBF fabricated and thermomechanically processed Ti-6Al-4V. Tangled dislocations in α' martensite can rearrange into dislocation arrays and form sub-grain boundaries during the α+β solution treatment[107]. In the

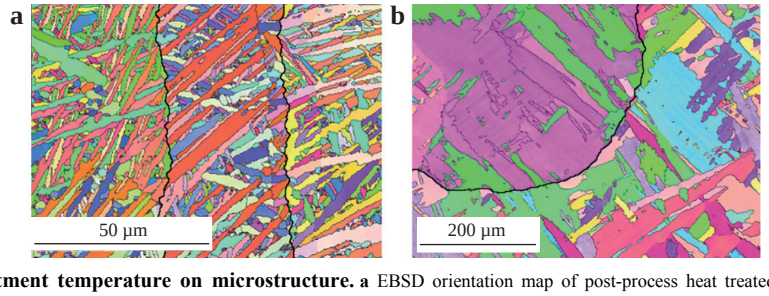

Fig. 10 Effect of heat treatment temperature on microstructure. a EBSD orientation map of post-process heat treated at sub-transus 850°C/2h/FC[84]. **b** EBSD orientation map of post-process heat treated at super-transus 1020°C/0.5h followed by sub-transus 730°C/2h/AC[84]. The deposition direction in both images is in vertical direction.

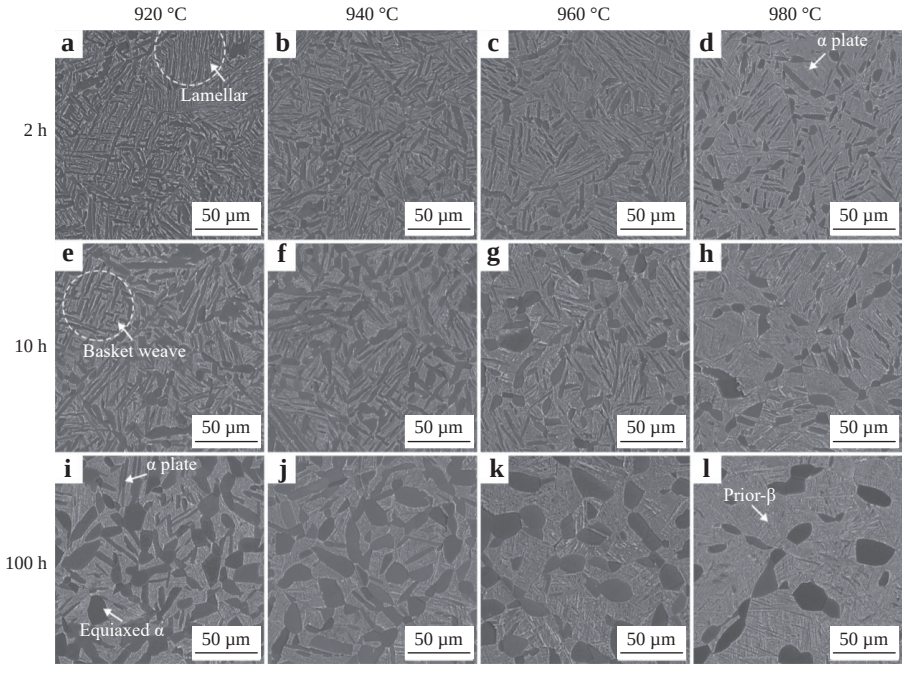

Fig. 11 Effect of sub-transus solution temperature and time on microstructure. SEM images of LPBF fabricated Ti-6Al-4V after different α+β STA heat treatments. The results show the effect of solution temperature and time on the microstructure evolution; all the solution treatments are followed by AC and a subsequent aging treatment at 700 °C/2 h/FC[105].

initial stage of globularization, dislocation arrays and sub-grain boundaries are the feasible locations for the boundary splitting process, which includes the growth of β phase into the sub-grain boundary (thermal grooving) and edge spheroidization at lamellae ends[109]. For a prolonged solution treatment, the globularization is driven by the second mechanism related to the α lamellae coarsening by termination migration consisting of mass transfer from curved surface to flat surfaces. This results in shorter and thicker α_p lamellae, which gradually change the lamellar morphology to a more equiaxed morphology[109].

In addition to α+β STA, a recent study has reported that a sub-transus cyclic heat treatment between 975 °C and 875 °C with slow heating and cooling rates for 24 h is able to provide a bi-modal microstructure with coarse globularized α_p and fine α_s within the β_t region[110]. The globularization mechanism during cyclic heat treatment differs from that mentioned in the α+β STA. The cyclic heat treatment leads to variations in the volume fraction of α and β, which promote α lamellae to β transformation in the heating cycle and facilitates β to a more equiaxed α transformation during the slow cooling cycle. During the heating cycle, the transformation from α to β also stimulates faster thermal grooving and boundary splitting processes[110].

Hot isostatic pressing

Typically, LPBF fabricated metals and alloys often contain defects such as gas pores, contour related pores, lack-of-fusion, keyhole pores, and partially melted powders[25,31,38,111]. These defects are detrimental to the fatigue properties and can affect the quality control of the LPBF process. As shown in Fig. 12, hot isostatic pressing (HIP) is an effective post-process method for tackling defects, including lack-of-fusion, keyhole, and gas pores, but it does not address pores connected to the surface as indicated by a few defects retained after HIP in Fig. 12a. Similar evidence of pore closure in HIP have been reported in other studies[112,113]. In addition, HIP can consolidate partially melted or unmelted powders[111]. A few studies have revealed that post-HIP annealing, including both sub-transus and super-transus heat treatments, re-opens the HIP 'closed' pores[111,114,115]. This indicates that these defects, containing Ar gas, are not eliminated by HIP and instead converted into small high-pressured pores, which are below the resolution of X-ray tomography.

The microstructure evolution during HIP is similar to that of heat-treated conditions. According to the ASTM standard for powder bed fusion fabricated Ti-6Al-4V[4], the recommended HIP scheme corresponds to 100 MPa at 895 to 955 °C for 3 to 4 h. Several studies have performed HIP at 900−950 °C/100-150 MPa/2-4 h[31,112,113,116], the resultant microstructure is mainly coarse α+β lamellar microstructure containing a few equiaxed α grains. For super-transus HIP, the prior-β grain will grow and the lath

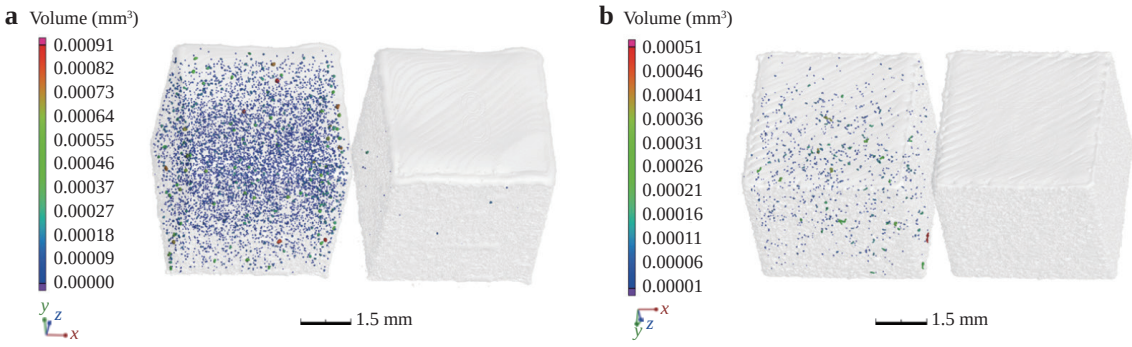

Fig. 12 Effect of HIP treatment on defects closure in LPBF fabricated Ti-6Al-4V. a Keyhole and gas pores closed by HIP. **b** Lack-of-fusion and gas pores closed by HIP. The voxel size is 5 μm for the X-ray tomography experiment[111].

thickness in the lamellar microstructure will be controlled by the cooling rate in the HIP cycle.

Microstructure and property

Tensile property

The most influential microstructural parameter that affects mechanical properties of LPBF fabricated lamellar structures is the α/α' width[35,64,76,96,117]. Under extremely fast cooled condition, the effective slip length for dislocation is limited to the individual martensite width rather than the α colony size in thermomechanically processed Ti-6Al-4V[1]. The relationship between the strength and α/α' width can be described by Hall-Petch relation as shown in Fig. 13a, in which a linear relationship can be established between the yield strength and the inverse square root of α/α' width. Such a relationship is still valid after post-process annealing and HIP treatments in α+β phase field according to Fig. 13a. In general, the ductility exhibits an inverse relationship with the yield strength as shown in Fig. 13b. The as-fabricated LPBF Ti-6Al-4V has a fine α' martensitic microstructure[118], which results in a high strength but low ductility as shown in Fig. 13b and Table 1. Post-process heat treatments and HIP can promote the martensite decomposition to α+β lamellae, which reduce the strength and increase the ductility. A recent study found that heat treated LPBF Ti-6Al-4V with an equilibrium microstructure possesses a superior ductility (elongation at fracture (El.) > 18%) similar to that of wrought Ti-6Al-4V[76]. Details on the martensite decomposition in post-process treatments have been summarized in the previous section of annealing. With respect to the lamellar microstructure, the overall trend is a higher heat/HIP treatment temperature (below the β transus) and/or a longer heat/HIP treatment time lead to a lower strength but a higher ductility as shown in Table 1.

In addition to the lamellar microstructure, another bi-lamellar/bi-modal microstructure can be achieved by post-process α+β STA and/or cyclic heat treatments which are described in the sections of solution treating and aging. As

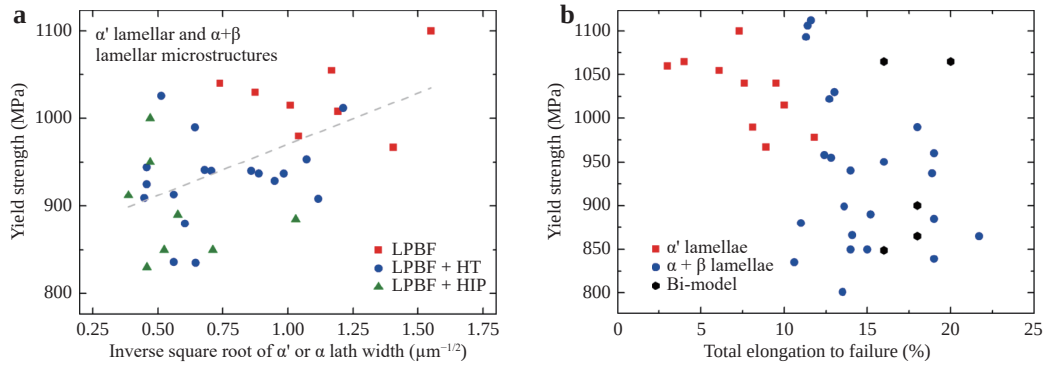

Fig. 13 The effect of microstructure on tensile properties. a A Hall-Petch relation between yield strength and the width of α' or α laths in Ti-6Al-4V with a lamellar microstructure fabricated by LPBF[31,54,63,64,94,112,119], LPBF and post-process heat treatment[16,31,120,121,60,63,76,83,84,94,103,119], and LPBF and post-process HIP[31,60,103,112,113,119,122]. **b** Yield strength vs. total elongation to failure for Ti-6Al-4V fabricated by LPBF with α ' lamellar microstructures[16,31,54,60,63,76,84,119,120], α+β lamellar microstructures[31,63,121,123,124,64,83,84,94,96,103,119,120], and bi-modal microstructures[102,104,110].

Table 1 Microstructure and mechanical properties of LPBF fabricated Ti-6Al-4V in as-printed, heat treated, and HIP treated conditions. Air Cool (AC) and Furnace Cool (FC) are cooling methods after heat treatment. YS-Yield Strength, UTS- Ultimate Tensile Strength, and El.- Elongation at fracture are measured tensile properties.

Condition & Ref.	Platform heating (°C)	Post-LPBF treatment	Microstructure	YS (MPa)	UTS (MPa)	El. (%)
As-LPBF [112]	100	–	α' lamellar	1 008 (V)	1 080 (V)	1.6 (V)
[116]	100	–	α' lamellar	–	1 315 ± 16 (V)	4.0 ± 1.2 (V)
[31]	70	–	α' lamellar	1 065 (H) 1 060 (V)	1 250 (H) 1 090 (V)	4 (H) 3 (V)
[120]	–	–	α' lamellar	1 055 (H)	1 098 (H)	6.1 (H)
[16]	500	–	α' lamellar	1 137 ± 20 (H) 926 ± 47 (V)	1 206 ± 8 (H) 1 116 ± 25 (V)	7.6 ± 2 (H) 1.7 ± 0.3 (V)
[54]	–	–	α' lamellar	1 140 ± 35 (H)	1 130 ± 31 (H)	7.6 ± 1.1 (H)
[76]	100	–	α' lamellar	1 040 ± 11 (H)	1 201 ± 10 (H)	9.5 ± 0.2 (H)
[63]	–	–	α' lamellar	978 ± 5 (H) 967 ± 10 (V)	1 143 ± 6 (H) 1 117 ± 3 (V)	11.8 ± 0.5 (H) 8.9 ±0.4 (V)
[64] .*	200	–	α+β lamellar	1 100 (V)	-	11.4 (V)
[96].*	200	–	α+β lamellar	1 022 ± 10 (V)	1 109 ± 10 (V)	12.7 ± 2.1 (V)
Heat treated [60]	–	670 °C/5 h	Partially decomposed α' lamellar	1 015 (V)	1 090 (V)	10 (V)
[103]	–	700 °C/2 h/FC	Partially decomposed α' lamellar	1 051 (V)	1 115 (V)	11.3 (V)
[63]	–	730 °C/2 h/FC	Partially decomposed α' lamellar	958 ± 6 (H) 937 ± 9 (V)	1 057 ± 8 (H) 1 052 ± 11 (V)	12.4 ± 0.7 (H) 9.6 ± 0.9 (V)
[76]	100	700 °C/2 h/FC	Partially decomposed α' lamellar	1 012 ± 9 (H)	1 109 ± 10 (H)	9.5 ± 0.2 (H)
[116]	100	800 °C/2 h/FC	Partially decomposed α' lamellar	-	1 228 ± 32 (V)	8.0 ± 1.5 (V)
[76]	100	800 °C/6 h/FC	α+β lamellar	937 ± 4 (H)	1 041 ± 5 (H)	19 ± 1 (H)
[124].**	–	920 °C/2 h/FC	α+β lamellar	850 (V)	933 (V)	15 (V)
[112]	100	1 050 °C/2 h/FC	α+β lamellar	798 (V)	956 (V)	11.6 (V)
[116]	100	1 050 °C/2 h/FC	α+β lamellar	–	986 ± 45 (V)	13.8 ± 0.8 (V)
HIP treated [103]	–	900 °C/100 MPa/2 h	α+β lamellar	885 (V)	973 (V)	19 (V)
[60]	–	920 °C/100 MPa/2 h	α+β lamellar	850 (V)	960 (V)	14 (V)
[116]	100	920 °C/100 MPa/2 h	α+β lamellar	–	1 089 ± 26 (V)	13.8 ± 1.3 (V)
[124].**	–	920 °C/120 MPa/2 h	α+β lamellar	839 (V)	941 (V)	19 (V)
[123] .**	–	930 °C/100 MPa/4 h	α+β lamellar	866 ± 50 (H) 865 ± 3 (V)	938 ± 43 (H) 936 ± 4 (V)	14 ± 2 (H) 22 ± 2 (V)
[116]	100	1 050 °C/100 MPa/2 h	α+β lamellar	–	1 007 ± 15 (V)	13.5 ± 0.7 (V)
Heat treated [104,125]	–	910-930 °C/8 h/WQ + 750 °C/4 h/FC	α+β bi-lamellar/bi-modal	~900 (V)	~950 (V)	~18 (V)
[110]	150	Thermal cycling between 975 °C and 875 °C/24 h/AC	α+β bi-modal	865 ± 19 (H) 849 ± 12 (V)	1 017 ± 16 (H) 1 004 ± 23 (V)	18 ± 1 (H) 16 ± 1 (V)
[102]	–	900 °C/100 h/AC	α+β bi-modal	~1 080 (V)	~1 120 (V)	~20 (V)

* Specimens were fabricated on support structures. ** Specimen surface was polished.

shown in Fig. 13b and Table 1, the bi-modal microstructure generally has an improved ductility without sacrificing strength when compared to the tensile properties of lamellar microstructure. The simultaneously enhanced strength and ductility are related to the fine α_s region and the coarse equiaxed α_p, respectively[107].

A further information that can be extracted from Fig. 13 is the scattered tensile property in LPBF fabricated Ti-6Al-4V, which can be attributed to the various specimen orientations, compositions, porosity levels, and microstructures resulting from different powder characteristics (size and composition), LPBF systems, exposure parameters/strategies, and post-LPBF treatments.

Despite the efforts on transforming a non-equilibrium α' martensitic microstructure into the an equilibrium α+β lamellar microstructure, a few studies have reported similar ductility in a fully martensitic microstructure when compared to that in an α+β microstructure[80,126–128]. In hot deformed Ti-6Al-4V, a rapid heating (> 50 °C/s) to the β phase field followed by water quenching lead to the formation of fine prior-β grains (~8 μm) containing only α' martensite, which simultaneously improves strength and ductility[126]. The increase in strength is attributed to the refinement in both martensite width and prior-β grain size, and the enhanced ductility is related to the reduced strain localization due to the shortened martensite, which is limited by the prior β grain size[126]. Two similar observations have been reported in LPBF fabricated Ti-6Al-4V, in which a fully martensitic lamellar microstructure with a fine prior-β grain width between 50-100 μm results in high strength and ductility[127,128]. For such an approach to achieve good tensile properties, the key is to have a small prior-β grain size[126]. It is known that the prior-β grain width is related to the hatch distance in laser continuous scan strategy and the point distance in pulsed laser strategy. A small hatch distance can provide a narrow prior-β width, but it sacrifices the productivity. In addition, cautiously controlled laser processing parameters are required to avoid the β formation during the in-process thermal cycling, because the low volume of thin β film causes stress concentration, which decreases ductility[127,128].

The mechanical properties of LPBF fabricated materials have been reported as anisotropic due to the columnar prior-β grains inclined close to the build direction[113,129,130] and the manufacturing defects[16,31]. In the former case, horizontally built samples generally have a higher strength but a lower ductility than those of vertically built samples, because the width of columnar β grains is aligned in the tensile direction of horizontal samples[113,129,130]. The situation is changed when lack-of-fusion defects present between deposited layers and scan vectors. Vilaro et al. have reported higher elongation in horizontally built samples than that in vertically built samples in as-fabricated and post-process heat treated LPBF Ti-6Al-4V[16]. The reason is that tension in the vertical direction tends to open the lack-of-fusion defects and results in a low ductility. Recently, a plasticity model has been developed to predict the stress state dependent anisotropic plasticity behavior of LPBF fabricated Ti-6Al-4V[131].

A recent study has revealed that β solution treatment can effectively mitigate the anisotropy in mechanical property due to the fact that β grains lost the columnar morphology after such a treatment[132]. However, the strength and ductility significantly decrease after β solution treatment, because excessive β grain growth occurs at temperature above the β transus[84,132].

Fatigue property

For LPBF fabricated Ti-6Al-4V, the fatigue performance is influenced by the surface finish, manufacturing defects, residual stress and microstructure[133,134]. The surface quality has been found to be the most crucial factor. Fig. 14b shows a rough as-built surface covered by partially melted powders. Without surface treatments, the fatigue performance of as-fabricated LPBF specimen is worse than that of the traditional cast products[133]. After surface treatment, the fatigue strength is significantly increased in LPBF Ti-6Al-4V with[57,58,60,103] and without post-process HIP treatments[58]. Fig. 14a shows that various surface treatments can improve the fatigue performance, and a reduced surface roughness of R_a = 0.3 μm (Fig. 14c), achieved by milling, improves the tension-tension (R = 0.1) high cycle fatigue (HCF) strength to 775 MPa[57], which is superior than that of wrought Ti-6Al-4V at 450–650 MPa[135]. Similarly, with respect to tension-compression fatigue (R = −1), Fig. 14d shows a similar observation that an improved surface quality increases the HCF strength, and a reduced surface roughness (R_a < 1 μm) provides a HCF strength comparable to that of wrought Ti-6Al-4V. This is consistent with the fractographs shown in Fig. 14e and f, which indicate that surface related defects are responsible for the inferior fatigue strength in the as-built sample, and fatigue crack initiation site is at the sample interior when the surface defects are removed by machining. The comparable or even higher HCF strength in improved surface conditions is because the LPBF fabricated Ti-6Al-4V has a much finer microstructure than wrought and cast Ti-6Al-4V, which means a short effective dislocation slip length and a high resistance to fatigue crack initiation.

If the defects are on the surface and/or at the sub-surface which are connected to the surface, then HIP cannot close such the surface related defects and does not improve the

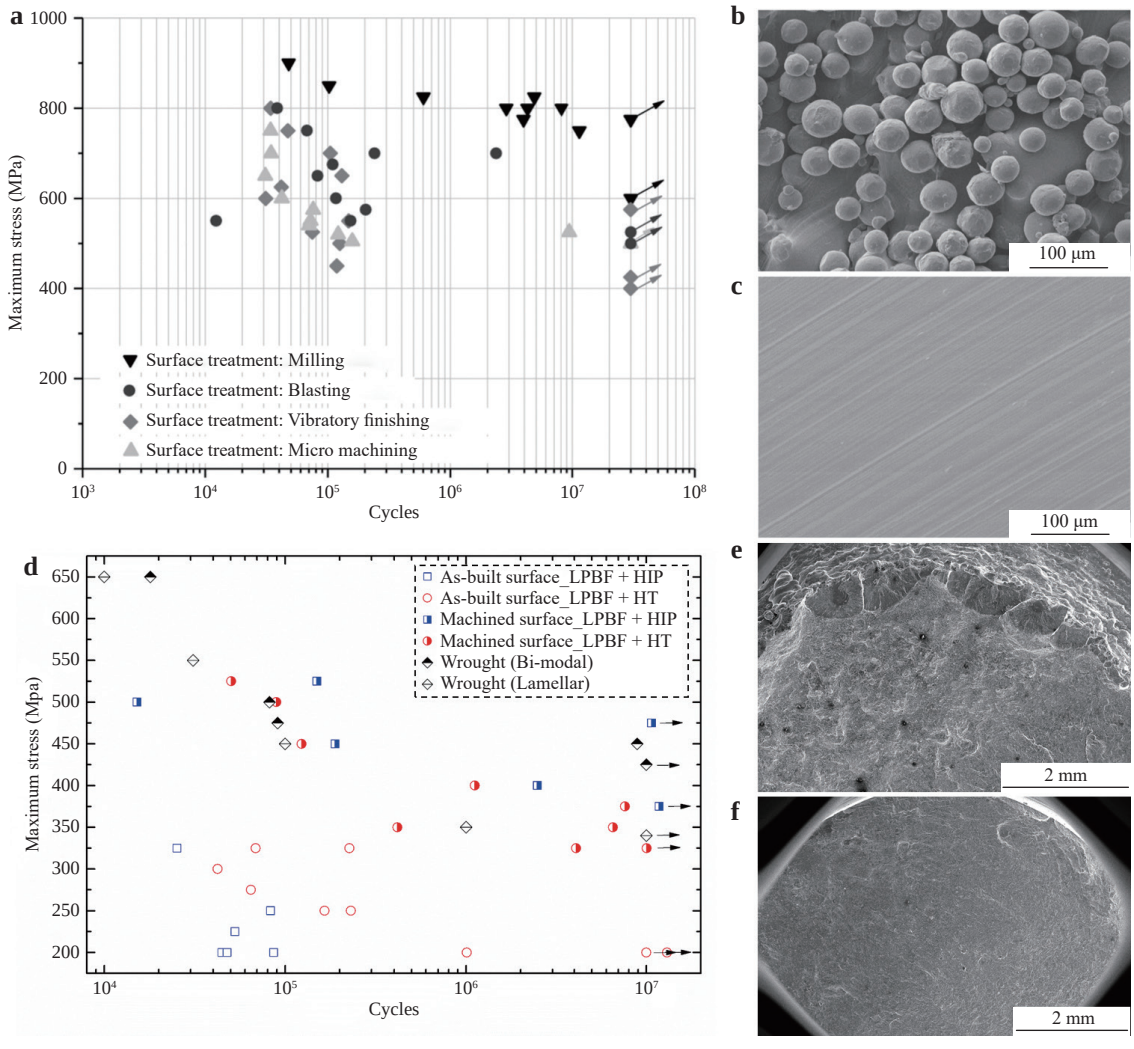

Fig. 14 Effect of surface finish on HCF strength. a Fatigue performance of post-process HIP treated LPBF Ti-6Al-4V after different surface treatments with an axial fatigue stress of R =0.1[57]. **b** SEM micrograph of as-built surface (R_a = 17.9 μm)[57]. **c** SEM image of milled surface (R_a = 0.3 μm)[57]. **d** Fatigue performance of post-process heat treated or HIP treated LPBF Ti-6Al-4V with an axial fatigue stress of R =-1[1,58]. **e** Fatigue fractograph of a sample with as-built surface (R_a > 7 μm)[58]. **f** Fatigue fractograph of a sample with machined surface (R_a < 1 μm)[58].

fatigue strength of samples with an as-built surface quality as shown in Fig. 14d. In contrast, internal defects can be addressed by post-process HIP, which has been summarised in the section of hot isostatic pressing. Fig. 14d shows that HIP improves the fatigue performance of machined samples (R_a < 1 μm), which is through eliminating the internal defects. In addition, HIP can effectively narrow down the fatigue data scatter[60]. As described in the section of residual stress, tensile residual stress, which accelerates the fatigue crack propagation and is detrimental to the fatigue properties[3], presents at the top and side surfaces of the part[50]. Therefore, surface peening treatments have been used to tackle the tensile residual stress, which result in a compressive stress below the surface and improves the fatigue strength[60,136].

For the influence of microstructures, previous investigations are mainly focused on the lamellar microstructure. In general, a finer microstructure has a higher fatigue strength. A sub-transus HIP treatment at 920 °C shows a better fatigue performance than the super-transus HIP treatment at 1 050 °C[116]. Similar observations has been reported in the heat treated conditions[116]. Whereas, the situation is different for fatigue crack growth (FCG). In the hypo-transitional region, FCG is generally influenced by the microstructure. A coarse microstructure has a higher fatigue crack threshold stress intensity factor (ΔK_{th}) and a slower FCG rate[137]. At the threshold range, a coarser lamellar microstructure displays a stronger ability to deflect cracks along the lath boundaries[137,138]. Even at a higher ΔK, crack deflection can be controlled by the colony/packet

size[138]. On the contrary, the cyclic plastic zone is sufficiently large in the hyper-transitional region, which exceeds the colony size, thus FCG is insensitive to the microstructure[138].

Fracture toughness and creep property

As described in tensile and fatigue properties, a fine microstructure generally provides high yield and HCF strengths. In contrast, a fine microstructure leads to a low fracture toughness[1]. For LPBF Ti-6Al-4V, the fracture toughness has been reported at values below 30 $MPa{\cdot}m^{-1/2}$ in the as-fabricated condition with α' martensitic microstructure[139]. This is lower than that of the wrought Ti-6Al-4V with a lamellar microstructure at 45-75 $MPa{\cdot}m^{-1/2}$ [1,3]. This is due to the extremely fine (sub-micro) and brittle α' in the as-fabricated condition. It has been found that post-process stress-relieving and annealing can improve the fracture toughness to approximately 50 $MPa{\cdot}m^{-1/2}$ [139,140], which is comparable to that of wrought alloys. In addition, anisotropic fracture toughness has been observed in both as-fabricated and post-process stress-relieved/annealed conditions, which is related to porosity levels and columnar β grains aligned along the build direction. A recent study has showed that a two-stage heat treatment of α+β STA effectively improves the fracture toughness to approximately 100 $MPa{\cdot}m^{-1/2}$ [138]. A short solution treatment at 920 °C followed by aging results in a coarse α+β Widmanstätten microstructure, and this microstructure can provide two benefits in terms of improving the fracture toughness. One is the α+β microstructure is more ductile than the α' martensitic microstructure, and the other is a coarser lamellar microstructure means a rougher crack front profile and an increased crack tortuosity[1,138].

In the temperature range between 450 °C and 650 °C, the as-fabricated Ti-6Al-4V has a comparable creep performance with that of the wrought Ti-6Al-4V[141]. After post-process heat treatments, a Widmanstätten microstructure showed a relatively lower creep strain and a lower steady-state creep rate than that in the as-fabricated condition. This indicates that the heat treated condition has a higher creep resistance[142]. This is due to the fact that the as-fabricated martensitic microstructure can be decomposed at creep testing temperatures, and such a microstructure evolution reduces the creep resistance[142]. The α/β interfaces in Widmanstätten microstructure act as obstacles to the dislocation glide during the creep deformation, which also improves the creep resistance[143,144].

Corrosion property

In titanium alloys, the corrosion resistance is attributed to the protective surface oxide film[1]. Therefore, the surface quality affects the corrosion performance of LPBF fabricated Ti-6Al-4V, and surface treatments can effectively improve the corrosion resistance by surface machining[145] and electropolishing[146]. For the influence of microstructure, metastable α' martensite is regarded as less corrosion resistant than the α phase, and the V-containing β phase is more corrosion resistant than α' martensite[147]. Therefore, as-fabricated LPBF Ti-6Al-4V has an inferior corrosion resistance (in 3.5 wt.% NaCl aqueous solution at room temperature) when compared with conventionally processed Ti-6Al-4V with an α+β lamellar microstructure due to the non-equilibrium α' martensitic microstructure[147,148]. The passive film thickness has been found to be thinner in laser fabricated Ti-6Al-4V than that in wrought counterpart, which also indicates a faster corrosion rate[149]. In terms of anisotropy, there is a negligible difference in corrosion properties between vertical and horizontal planes in 3.5 wt.% NaCl aqueous solution, while anisotropic corrosion behavior has been observed in a harsher environment of 1 M HCl aqueous solution, and the authors have related the anisotropy to different β volume fractions on different orientations[150].

After post-process heat treatments, previous studies showed two distinctly different corrosion phenomena. A recent study has reported that both sub-transus and super-transus heat treatments deteriorated the corrosion resistance in 3.5 wt.% NaCl aqueous solution at room temperature due to the increased grain size[151]. While, other studies have suggested that post-process heat treatments improve the corrosion resistance in Ringer's solution at 37 °C[152] and in 3.5 wt.% NaCl aqueous solution at room temperature[147]. This is attributed to the limited element segregation in the μm-sized α+β lamellar microstructure after the heat treatment, which mitigates the galvanic corrosion between α and β phases[147]. Nevertheless, further investigations on the corrosion performance of SLM-produced Ti-6Al-4V are required to understand the influence of post-process heat treatments.

Conclusion

In this paper, the LPBF process, post-process treatments, microstructures, and properties of LPBF fabricated Ti-6Al-4V have been briefly reviewed. At the beginning, the influences of processing parameters on the defect formation, residual stress, and surface roughness are presented. This is followed by the as-fabricated microstructure and its evolution during the in-process and post-process treatments. Lastly, the effects of microstructure, defects, and surface roughness on tensile, fatigue, fracture toughness, and creep properties are discussed. A summary of specific findings is provided

below:

- The formation of defects and surface quality can be controlled by tuning the processing parameters and scan strategies.
- The residual stress and pores in the as-fabricated Ti-6Al-4V can be addressed via post-process HIP treatments.
- The as-fabricated Ti-6Al-4V generally has a hierarchical microstructure containing textured prior-β grains that are aligned close to the build direction and intragranular hexagonal α' martensitic microstructure. In addition, a few studies have observed a small amount of β, α_2, and orthorhombic α'' martensite in the as-fabricated condition.
- The microstructure evolution, including martensite decomposition and formation of lamellar and/or bi-modal α+β microstructures, can be realized via in-process thermal cycling and post-process treatments.
- For the lamellar microstructure, the yield strength follows a Hall-Petch relationship with the lamellar width in the as-fabricated and post-process treated samples. The typical trade-off between strength and ductility is observed within the sample with a lamellar microstructure. In contrast, the bi-modal microstructure can provide a simultaneous enhancement in strength and ductility.
- After surface treatments, the fine microstructure in as-LPBF and post-process treated conditions leads to a high HCF strength. In contrast, a coarse α+β Widmanstätten microstructure is preferred for obtaining good fracture toughness and creep properties.
- In terms of corrosion resistance, the as-fabricated Ti-6Al-4V has an inferior corrosion performance than that of wrought counterpart, which is related to the metastable α' martensitic microstructure. A more detailed understanding of the influence of post-process heat treatments on the corrosion behavior is required.
- Most post-process treatments, including heat treatments, HIP, and surface treatments, lead to comparable or even superior tensile, fatigue, fracture toughness, and creep properties than those of cast and/or wrought Ti-6Al-4V.

Outlook

In principle, LPBF fabricated Ti-6Al-4V has great advantages in preparing complex near-net shape parts and reducing lead times. However, there is still a gap between the current research and the aforementioned advantages. For example, surface roughness and internal defects require post-process surface treatments and HIP to address. Additionally, disadvantages of anisotropic microstructure and properties must be considered, and the mitigation of anisotropy requires further investigation.

In terms of microstructure and properties, LPBF fabricated Ti-6Al-4V possesses a fine microstructure, which offers great advantages, including superior tensile and HCF strengths. However, a fine microstructure is not favorable for fracture toughness and creep resistance. A careful microstructure design through post-process treatments is required for specific applications.

In contrast to the inverse relationship between tensile strength and ductility in the lamellar microstructure, the bi-modal microstructure shows a great potential in terms of achieving satisfied strength and ductility. In addition, the bi-modal microstructure shows a higher HCF strength, a slower fatigue crack propagation rate of microcracks, and a higher LCF strength in wrought and cast alloys. As a two-step α+β STA treatment is generally used to obtain a bi-modal microstructure, the alloy element partitioning effect inevitably occurs. Future studies are required to understand the effect of strength difference between the initially formed α_p and the subsequently formed α_s on properties at a fine scale in LPBF fabricated Ti-6Al-4V.

Acknowledgements

This work is funded by Australian Research Council IH130100008 "Industrial Transformation Research Hub for Transforming Australia's Manufacturing Industry through High Value Additive Manufacturing". The authors gratefully acknowledge useful discussions with Kai Zhang and Jianwen Liu from the University of Shanghai for Science and Technology.

Author details

[1]Department of Materials, The University of Manchester, Oxford Road, Manchester, M13 9PL, UK. [2]Monash Centre for Additive Manufacturing, Monash University, VIC 3800, Australia. [3]Department of Materials Science and Engineering, Monash University, VIC 3800

Author contributions

Sheng Cao: Conceptualisation (lead) and Writing-original draft (lead). Yichao Zou: Writing-review & editing (equal). Chao Voon Samuel Lim: Writing-review & editing (equal). Xinhua Wu: Writing-review & editing (equal).

Conflict of interest

The authors have no competing interests to declare.

Received: 22 January 2021 Revised: 15 July 2021 Accepted: 16 July 2021
Accepted article preview online: 20 July 2021
Published online: 13 August 2021

References

1. Lütjering, G. & Williams, J. C. Titanium. 2nd edn. (Berlin: Springer, 2007).
2. Leyens, C. & Peters, M. Titanium and Titanium Alloys. (Weinheim: Wiley-VCH, 2003).
3. Boyer, R, Welsch, G. & Collings, E. W. Materials Properties Handbook: Titanium Alloys. (Materials Park: ASM International, 1994).
4. ASTM F2924-14. Standard specification for additive manufacturing

titanium-6 aluminum-4 vanadium with powder bed fusion. ASTM International, West Conshohocken, PA, USA 2014.
5. AMS4998E. Aerospace Material Specification, Titanium Alloy Powder 6Al-4V. SAE International, Warrendale, PA, USA, 2017,
6. Burgers, W. G. On the process of transition of the cubic-body-centered modification into the hexagonal-close-packed modification of zirconium. *Physica* **1**, 561-586 (1934).
7. Ramachandra, C. & Singh, V. Precipitation of the ordered Ti_3Al phase in alloy Ti-6.3Al-2Zr-3.3Mo-O.3OSi. *Scripta Metallurgica* **20**, 509-512 (1986).
8. Radecka, A. et al. The formation of ordered clusters in Ti-7Al and Ti-6Al-4V. *Acta Materialia* **112**, 141-149 (2016).
9. Fitzner, A. et al. The effect of aluminium on twinning in binary alpha-titanium. *Acta Materialia* **103**, 341-351 (2016).
10. Williams, J. C., Thompson, A. W. & Baggerly, R. G. Accurate description of slip character. *Scripta Metallurgica* **8**, 625-630 (1974).
11. Williams, J. C., Sommer, A. W. & Tung, P. P. The influence of oxygen concentration on the internal stress and dislocation arrangements in α titanium. *Metallurgical and Materials Transactions B* **3**, 2979-2984 (1972).
12. Cao, S. et al. Effects of microtexture and Ti_3Al (α_2) precipitates on stress-corrosion cracking properties of a Ti-8Al-1Mo-1V alloy. *Corrosion Science* **116**, 22-33 (2017).
13. Kenel, C. et al. In situ investigation of phase transformations in Ti-6Al-4V under additive manufacturing conditions combining laser melting and high-speed micro-X-ray diffraction. *Scientific Reports* **7**, 16358 (2017).
14. Neelakantan, S. et al. Prediction of the martensite start temperature for β titanium alloys as a function of composition. *Scripta Materialia* **60**, 611-614 (2009).
15. Ahmed, T. & Rack, H. J. Phase transformations during cooling in α+β titanium alloys. *Materials Science and Engineering: A* **243**, 206-211 (1998).
16. Vilaro, T., Colin, C. & Bartout, J. D. As-fabricated and heat-treated microstructures of the Ti-6Al-4V alloy processed by selective laser melting. *Metallurgical and Materials Transactions A* **42**, 3190-3199 (2011).
17. Banerjee, D. & Williams, J. C. Perspectives on titanium science and technology. *Acta Materialia* **61**, 844-879 (2013).
18. Edwards, P. & Ramulu, M. Fatigue performance evaluation of selective laser melted Ti–6Al–4V. *Materials Science and Engineering: A* **598**, 327-337 (2014).
19. Jia, Q. B. et al. Towards a high strength aluminium alloy development methodology for selective laser melting. *Materials & Design* **174**, 107775 (2019).
20. Brandt, M. The role of lasers in additive manufacturing. in Laser Additive Manufacturing: Materials, Design, Technologies, and Applications (ed Brandt, M.) (Amsterdam: Elsevier, 2017).
21. Kruth, J. P. et al. Binding mechanisms in selective laser sintering and selective laser melting. *Rapid Prototyping Journal* **11**, 26-36 (2005).
22. Sing, S. L. & Yeong, W. Y. Laser powder bed fusion for metal additive manufacturing: perspectives on recent developments. *Virtual and Physical Prototyping* **15**, 359-370 (2020).
23. Strondl, A. et al. Characterization and control of powder properties for additive manufacturing. *JOM* **67**, 549-554 (2015).
24. Shipley, H. et al. Optimisation of process parameters to address fundamental challenges during selective laser melting of Ti-6Al-4V: a review. *International Journal of Machine Tools and Manufacture* **128**, 1-20 (2018).
25. Gong, H. J. et al. Analysis of defect generation in Ti–6Al–4V parts made using powder bed fusion additive manufacturing processes. *Additive Manufacturing* **1-4**, 87-98 (2014).
26. King, W. E. et al. Laser powder bed fusion additive manufacturing of metals; physics, computational, and materials challenges. *Applied Physics Reviews* **2**, 41304 (2015).
27. Zhang, L. C. et al. Manufacture by selective laser melting and mechanical behavior of a biomedical Ti–24Nb–4Zr–8Sn alloy. *Scripta Materialia* **65**, 21-24 (2011).
28. Promoppatum, P., Onler, R. & Yao, S. C. Numerical and experimental investigations of micro and macro characteristics of direct metal laser sintered Ti-6Al-4V products. *Journal of Materials Processing Technology* **240**, 262-273 (2017).
29. He, Y. N. et al. Melt pool geometry and microstructure of Ti6Al4V with B additions processed by selective laser melting additive manufacturing. *Materials & Design* **183**, 108126 (2019).
30. Bertoli, U. S. et al. On the limitations of volumetric energy density as a design parameter for selective laser melting. *Materials & Design* **113**, 331-340 (2017).
31. Cao, S. et al. Defect, microstructure, and mechanical property of Ti-6Al-4V alloy fabricated by high-power selective laser melting. *JOM* **69**, 2684-2692 (2017).
32. Attar, H. et al. Comparative study of commercially pure titanium produced by laser engineered net shaping, selective laser melting and casting processes. *Materials Science and Engineering: A* **705**, 385-393 (2017).
33. Cunningham, R. et al. Synchrotron-Based X-ray microtomography characterization of the effect of processing variables on porosity formation in laser power-bed additive manufacturing of Ti-6Al-4V. *JOM* **69**, 479-484 (2017).
34. Chen, G. et al. A comparative study of Ti-6Al-4V powders for additive manufacturing by gas atomization, plasma rotating electrode process and plasma atomization. *Powder Technology* **333**, 38-46 (2018).
35. Singla, A. K. et al. Selective laser melting of Ti6Al4V alloy: process parameters, defects and post-treatments. *Journal of Manufacturing Processes* **64**, 161-187 (2021).
36. Kasperovich, G. et al. Correlation between porosity and processing parameters in TiAl6V4 produced by selective laser melting. *Materials & Design* **105**, 160-170 (2016).
37. DebRoy, T. et al. Additive manufacturing of metallic components–Process, structure and properties. *Progress in Materials Science* **92**, 112-224 (2018).
38. Thijs, L. et al. A study of the microstructural evolution during selective laser melting of Ti-6Al-4V. *Acta Materialia* **58**, 3303-3312 (2010).
39. Qian, L. et al. Influence of position and laser power on thermal history and microstructure of direct laser fabricated Ti–6Al–4V samples. *Materials Science and Technology* **21**, 597-605 (2005).
40. Pantawane, M. V. et al. Rapid thermokinetics driven nanoscale vanadium clustering within martensite laths in laser powder bed fused additively manufactured Ti6Al4V. *Materials Research Letters* **8**, 383-389 (2020).
41. Bertoli, U. S. et al. In-situ characterization of laser-powder interaction and cooling rates through high-speed imaging of powder bed fusion additive manufacturing. *Materials & Design* **135**, 385-396 (2017).
42. Li, Y. L. & Gu, D. D. Parametric analysis of thermal behavior during selective laser melting additive manufacturing of aluminum alloy powder. *Materials & Design* **63**, 856-867 (2014).
43. Wang, J. C. et al. Selective laser melting of Ti–35Nb composite from elemental powder mixture: microstructure, mechanical behavior and corrosion behavior. *Materials Science and Engineering: A* **760**, 214-224 (2019).
44. Wang, J. C. et al. Microstructural homogeneity and mechanical behavior of a selective laser melted Ti-35Nb alloy produced from an elemental powder mixture. *Journal of Materials Science & Technology*

61, 221-233 (2021).
45. Hocine, S. et al. Operando X-ray diffraction during laser 3D printing. *Materials Today* **34**, 30-40 (2020).
46. Ganeriwala, R. K. et al. Evaluation of a thermomechanical model for prediction of residual stress during laser powder bed fusion of Ti-6Al-4V. *Additive Manufacturing* **27**, 489-502 (2019).
47. Yu, W. H. et al. Particle-reinforced metal matrix nanocomposites fabricated by selective laser melting: a state of the art review. *Progress in Materials Science* **104**, 330-379 (2019).
48. Song, J. et al. Role of scanning strategy on residual stress distribution in Ti-6Al-4V alloy prepared by selective laser melting. *Optik* **170**, 342-352 (2018).
49. Mercelis, P. & Kruth, J. P. Residual stresses in selective laser sintering and selective laser melting. *Rapid Prototyping Journal* **12**, 254-265 (2006).
50. Levkulich, N. C. et al. The effect of process parameters on residual stress evolution and distortion in the laser powder bed fusion of Ti-6Al-4V. *Additive Manufacturing* **28**, 475-484 (2019).
51. Ahmad, B. et al. Residual stress evaluation in selective-laser-melting additively manufactured titanium (Ti-6Al-4V) and inconel 718 using the contour method and numerical simulation. *Additive Manufacturing* **22**, 571-582 (2018).
52. Ali, H., Ghadbeigi, H. & Mumtaz, K. Effect of scanning strategies on residual stress and mechanical properties of Selective Laser Melted Ti6Al4V. *Materials Science and Engineering: A* **712**, 175-187 (2018).
53. Vandenbroucke, B. & Kruth, J. P. Selective laser melting of biocompatible metals for rapid manufacturing of medical parts. *Rapid Prototyping Journal* **13**, 196-203 (2007).
54. Shi, X. Z. et al. Effect of high layer thickness on surface quality and defect behavior of Ti-6Al-4V fabricated by selective laser melting. *Optics & Laser Technology* **132**, 106471 (2020).
55. Brika, S. E. et al. Influence of particle morphology and size distribution on the powder flowability and laser powder bed fusion manufacturability of Ti-6Al-4V alloy. *Additive Manufacturing* **31**, 100929 (2020).
56. Chen, Z. E. et al. Surface roughness of Selective Laser Melted Ti-6Al-4V alloy components. *Additive Manufacturing* **21**, 91-103 (2018).
57. Bagehorn, S., Wehr, J. & Maier, H. J. Application of mechanical surface finishing processes for roughness reduction and fatigue improvement of additively manufactured Ti-6Al-4V parts. *International Journal of Fatigue* **102**, 135-142 (2017).
58. Chen, Z. E. et al. Surface roughness and fatigue properties of selective laser melted Ti-6Al-4V alloy. in Additive Manufacturing for the Aerospace Industry (eds Froes, F. & Boyer, R.) (Amsterdam: Elsevier, 2019), 283-299.
59. Vaidya, R. & Anand, S. Optimum support structure generation for additive manufacturing using unit cell structures and support removal constraint. *Procedia Manufacturing* **5**, 1043-1059 (2016).
60. Benedetti, M. et al. The effect of post-sintering treatments on the fatigue and biological behavior of Ti-6Al-4V ELI parts made by selective laser melting. *Journal of the Mechanical Behavior of Biomedical Materials* **71**, 295-306 (2017).
61. Kumar, P. & Ramamurty, U. High cycle fatigue in selective laser melted Ti-6Al-4V. *Acta Materialia* **194**, 305-320 (2020).
62. Simonelli, M., Tse, Y. Y. & Tuck, C. On the texture formation of selective laser melted Ti-6Al-4V. *Metallurgical and Materials Transactions A* **45**, 2863-2872 (2014).
63. Simonelli, M., Tse, Y. Y. & Tuck, C. Effect of the build orientation on the mechanical properties and fracture modes of SLM Ti-6Al-4V. *Materials Science and Engineering: A* **616**, 1-11 (2014).
64. Xu, W. et al. Additive manufacturing of strong and ductile Ti-6Al-4V by selective laser melting via in situ martensite decomposition. *Acta Materialia* **85**, 74-84 (2015).
65. Sallica-Leva, E. et al. Ductility improvement due to martensite α' decomposition in porous Ti–6Al–4V parts produced by selective laser melting for orthopedic implants. *Journal of the Mechanical Behavior of Biomedical Materials* **54**, 149-158 (2016).
66. Murr, L. E. et al. Microstructure and mechanical behavior of Ti-6Al-4V produced by rapid-layer manufacturing, for biomedical applications. *Journal of the Mechanical Behavior of Biomedical Materials* **2**, 20-32 (2009).
67. Wu, X. H. et al. Microstructures of laser-deposited Ti-6Al-4V. *Materials & Design* **25**, 137-144 (2004).
68. Yin, J. et al. Microstructure and mechanical property of selective laser melted Ti6Al4V dependence on laser energy density. *Rapid Prototyping Journal* **23**, 217-226 (2017).
69. Voisin, T. et al. Defects-dictated tensile properties of selective laser melted Ti-6Al-4V. *Materials & Design* **158**, 113-126 (2018).
70. Zhang, D. C. et al. Effect of heat treatment on the tensile behavior of selective laser melted Ti-6Al-4V by in situ X-ray characterization. *Acta Materialia* **189**, 93-104 (2020).
71. Barriobero-Vila, P. et al. Inducing stable α + β microstructures during selective laser melting of Ti-6Al-4V using intensified intrinsic heat treatments. *Materials* **10**, 268 (2017).
72. Yang, J. J. et al. Formation and control of martensite in Ti-6Al-4V alloy produced by selective laser melting. *Materials & Design* **108**, 308-318 (2016).
73. Haubrich, J. et al. The role of lattice defects, element partitioning and intrinsic heat effects on the microstructure in selective laser melted Ti-6Al-4V. *Acta Materialia* **167**, 136-148 (2019).
74. Simonelli, M., Tse, Y. Y. & Tuck, C. Microstructure of Ti-6Al-4V produced by selective laser melting. *Journal of Physics: Conference Series* **371**, 012084 (2012).
75. Kumar, M. A. et al. Role of microstructure on twin nucleation and growth in HCP titanium: a statistical study. *Acta Materialia* **148**, 123-132 (2018).
76. Cao, S. et al. Role of martensite decomposition in tensile properties of selective laser melted Ti-6Al-4V. *Journal of Alloys and Compounds* **744**, 357-363 (2018).
77. Xie, Z. Y. et al. Effects of selective laser melting build orientations on the microstructure and tensile performance of Ti–6Al–4V alloy. *Materials Science and Engineering: A* **776**, 139001 (2020).
78. Kazantseva, N. et al. Martensitic transformations in Ti-6Al-4V (ELI) alloy manufactured by 3D Printing. *Materials Characterization* **146**, 101-112 (2018).
79. Krakhmalev, P. et al. Deformation behavior and microstructure of Ti6Al4V manufactured by SLM. *Physics Procedia* **83**, 778-788 (2016).
80. Matsumoto, H. et al. Room-temperature ductility of Ti-6Al-4V alloy with α' martensite microstructure. *Materials Science and Engineering: A* **528**, 1512-1520 (2011).
81. Cao, S. et al. On the role of cooling rate and temperature in forming twinned α' martensite in Ti–6Al–4V. *Journal of Alloys and Compounds* **813**, 152247 (2020).
82. Yang, J. J. et al. Role of molten pool mode on formability, microstructure and mechanical properties of selective laser melted Ti-6Al-4V alloy. *Materials & Design* **110**, 558-570 (2016).
83. Facchini, L. et al. Ductility of a Ti-6Al-4V alloy produced by selective laser melting of prealloyed powders. *Rapid Prototyping Journal* **16**, 450-459 (2010).
84. Vrancken, B. et al. Heat treatment of Ti6Al4V produced by Selective Laser Melting: microstructure and mechanical properties. *Journal of Alloys and Compounds* **541**, 177-185 (2012).
85. Kruth, J. P. et al. Assessing and comparing influencing factors of residual stresses in selective laser melting using a novel analysis

method. *Proceedings of the Institution of Mechanical Engineers, Part B: Journal of Engineering Manufacture* **226**, 980-991 (2012).
86. Ali, H. et al. In-situ residual stress reduction, martensitic decomposition and mechanical properties enhancement through high temperature powder bed pre-heating of Selective Laser Melted Ti6Al4V. *Materials Science and Engineering: A* **695**, 211-220 (2017).
87. Kaschel, F. R. et al. Mechanism of stress relaxation and phase transformation in additively manufactured Ti-6Al-4V via *in situ* high temperature XRD and TEM analyses. *Acta Materialia* **188**, 720-732 (2020).
88. Papadakis, L., Chantzis, D. & Salonitis, K. On the energy efficiency of pre-heating methods in SLM/SLS processes. *The International Journal of Advanced Manufacturing Technology* **95**, 1325-1338 (2018).
89. Malý, M. et al. Effect of process parameters and high-temperature preheating on residual stress and relative density of Ti6Al4V processed by selective laser melting. *Materials* **12**, 930 (2019).
90. Yan, M. et al. A transmission electron microscopy and three-dimensional atom probe study of the oxygen-induced fine microstructural features in as-sintered Ti–6Al–4V and their impacts on ductility. *Acta Materialia* **68**, 196-206 (2014).
91. Alamos, F. J. et al. Effect of powder reuse on mechanical properties of Ti-6Al-4V produced through selective laser melting. *International Journal of Refractory Metals and Hard Materials* **91**, 105273 (2020).
92. Xu, Y. L. et al. Microstructural tailoring of as-selective laser melted Ti6Al4V alloy for high mechanical properties. *Journal of Alloys and Compounds* **816**, 152536 (2020).
93. Dahotre, N. B. & Harimkar, S. P. Laser Fabrication and Machining of Materials. (New York: Springer Science, 2008)
94. Xu, W. et al. Ti-6Al-4V additively manufactured by selective laser melting with superior mechanical properties. *JOM* **67**, 668-673 (2015).
95. Lui, E. W. et al. New development in selective laser melting of Ti–6Al–4V: a wider processing window for the achievement of fully lamellar α + β microstructures. *JOM* **69**, 2679-2683 (2017).
96. Xu, W. et al. *In situ* tailoring microstructure in additively manufactured Ti-6Al-4V for superior mechanical performance. *Acta Materialia* **125**, 390-400 (2017).
97. Beese, A. M. & Carroll, B. E. Review of mechanical properties of Ti-6Al-4V made by laser-based additive manufacturing using powder feedstock. *JOM* **68**, 724-734 (2016).
98. Baker, A. H., Collins, P. C. & Williams, J. C. New nomenclatures for heat treatments of additively manufactured titanium alloys. *JOM* **69**, 1221-1227 (2017).
99. Wu, S. Q. et al. Microstructural evolution and microhardness of a selective-laser-melted Ti-6Al-4V alloy after post heat treatments. *Journal of Alloys and Compounds* **672**, 643-652 (2016).
100. Motyka, M. et al. Decomposition of deformed α′(α″) martensitic phase in Ti–6Al–4V alloy. *Materials Science and Technology* **35**, 260-272 (2019).
101. Cao, S. et al. Static coarsening behaviour of lamellar microstructure in selective laser melted Ti–6Al–4V. *Journal of Materials Science & Technology* **35**, 1578-1586 (2019).
102. Kusano, M. et al. Tensile properties prediction by multiple linear regression analysis for selective laser melted and post heat-treated Ti-6Al-4V with microstructural quantification. *Materials Science and Engineering: A* **787**, 139549 (2020).
103. Kasperovich, G. & Hausmann, J. Improvement of fatigue resistance and ductility of TiAl6V4 processed by selective laser melting. *Journal of Materials Processing Technology* **220**, 202-214 (2015).
104. Ter Haar, G. M. & Becker, T. H. Selective laser melting produced Ti-6Al-4V: post-process heat treatments to achieve superior tensile properties. *Materials* **11**, 146 (2018).
105. Miyazaki, S. et al. Image segmentation and analysis for microstructure and property evaluations on Ti–6Al–4V fabricated by selective laser melting. *Materials Transactions* **60**, 561-568 (2019).
106. De Formanoir, C. et al. Micromechanical behavior and thermal stability of a dual-phase α+α' titanium alloy produced by additive manufacturing. *Acta Materialia* **162**, 149-162 (2019).
107. Zhao, Z. et al. Achieving superior ductility for laser solid formed extra low interstitial Ti-6Al-4V titanium alloy through equiaxial alpha microstructure. *Scripta Materialia* **146**, 187-191 (2018).
108. Wang, J. et al. Effects of subtransus heat treatments on microstructure features and mechanical properties of wire and arc additive manufactured Ti–6Al–4V alloy. *Materials Science and Engineering: A* **776**, 139020 (2020).
109. Stefansson, N. & Semiatin, S. L. Mechanisms of globularization of Ti-6Al-4V during static heat treatment. *Metallurgical and Materials Transactions A* **34**, 691-698 (2003).
110. Sabban, R. et al. Globularization using heat treatment in additively manufactured Ti-6Al-4V for high strength and toughness. *Acta Materialia* **162**, 239-254 (2019).
111. Du Plessis, A. & Macdonald, E. Hot isostatic pressing in metal additive manufacturing: X-ray tomography reveals details of pore closure. *Additive Manufacturing* **34**, 101191 (2020).
112. Leuders, S. et al. On the mechanical behaviour of titanium alloy TiAl6V4 manufactured by selective laser melting: Fatigue resistance and crack growth performance. *International Journal of Fatigue* **48**, 300-307 (2013).
113. Qiu, C. L., Adkins, N. J. E. & Attallah, M. M. Microstructure and tensile properties of selectively laser-melted and of HIPed laser-melted Ti-6Al-4V. *Materials Science and Engineering: A* **578**, 230-239 (2013).
114. Cunningham, R. et al. Analyzing the effects of powder and post-processing on porosity and properties of electron beam melted Ti-6Al-4V. *Materials Research Letters* **5**, 516-525 (2017).
115. Tammas-Williams, S. et al. Porosity regrowth during heat treatment of hot isostatically pressed additively manufactured titanium components. *Scripta Materialia* **122**, 72-76 (2016).
116. Leuders, S. et al. On the fatigue properties of metals manufactured by selective laser melting–The role of ductility. *Journal of Materials Research* **29**, 1911-1919 (2014).
117. Baufeld, B., Van Der Biest, O. & Gault, R. Additive manufacturing of Ti–6Al–4V components by shaped metal deposition: microstructure and mechanical properties. *Materials & Design* **31**, S106-S111 (2010).
118. Zhang, L. C. & Attar, H. Selective laser melting of titanium alloys and titanium matrix composites for biomedical applications: a review . *Advanced Engineering Materials* **18**, 463-475 (2016).
119. Benedetti, M. et al. Low- and high-cycle fatigue resistance of Ti-6Al-4V ELI additively manufactured via selective laser melting: mean stress and defect sensitivity. *International Journal of Fatigue* **107**, 96-109 (2018).
120. Yang, Y. et al. Crystallographic features of α variants and β phase for Ti-6Al-4V alloy fabricated by selective laser melting. *Materials Science and Engineering: A* **707**, 548-558 (2017).
121. Frkan, M. et al. Microstructure and fatigue performance of SLM-fabricated Ti6Al4V alloy after different stress-relief heat treatments. *Transportation Research Procedia* **40**, 24-29 (2019).
122. Zhou, B. et al. A study of the microstructures and mechanical properties of Ti6Al4V fabricated by SLM under vacuum. *Materials Science and Engineering: A* **724**, 1-10 (2018).
123. Jamshidi, P. et al. Selective laser melting of Ti-6Al-4V: the impact of post-processing on the tensile, fatigue and biological properties for medical implant applications. *Materials* **13**, 2813 (2020).
124. Yan, X. C. et al. Effect of heat treatment on the phase transformation and mechanical properties of Ti6Al4V fabricated by selective laser

melting. *Journal of Alloys and Compounds* **764**, 1056-1071 (2018).
125. Ter Haar, G. M. Selective Laser Melting-produced Ti6Al4V: Influence of annealing strategies on crystallographic microstructure and tensile behaviour. MEng thesis, Stellenbosch University (2017).
126. Chong, Y. et al. Mechanical properties of fully martensite microstructure in Ti-6Al-4V alloy transformed from refined beta grains obtained by rapid heat treatment (RHT). *Scripta Materialia* **138**, 66-70 (2017).
127. Zafari, A. & Xia, K. High ductility in a fully martensitic microstructure: a paradox in a Ti alloy produced by selective laser melting. *Materials Research Letters* **6**, 627-633 (2018).
128. Zafari, A., Barati, M. R. & Xia, K. Controlling martensitic decomposition during selective laser melting to achieve best ductility in high strength Ti-6Al-4V. *Materials Science and Engineering: A* **744**, 445-455 (2019).
129. Carroll, B. E., Palmer, T. A. & Beese, A. M. Anisotropic tensile behavior of Ti-6Al-4V components fabricated with directed energy deposition additive manufacturing. *Acta Materialia* **87**, 309-320 (2015).
130. Wilson-Heid, A. E. et al. Quantitative relationship between anisotropic strain to failure and grain morphology in additively manufactured Ti-6Al-4V. *Materials Science and Engineering: A* **706**, 287-294 (2017).
131. Wilson-Heid, A. E., Qin, S. P. & Beese, A. M. Anisotropic multiaxial plasticity model for laser powder bed fusion additively manufactured Ti-6Al-4V. *Materials Science and Engineering: A* **738**, 90-97 (2018).
132. Ter Haar G. M. & Becker T. H. The influence of microstructural texture and prior beta grain recrystallisation on the deformation behaviour of laser powder bed fusion produced Ti–6Al–4V. *Materials Science and Engineering: A* **814**, 141185 (2021).
133. Li, P. et al. Critical assessment of the fatigue performance of additively manufactured Ti-6Al-4V and perspective for future research. *International Journal of Fatigue* **85**, 130-143 (2016).
134. Günther, J. et al. On the effect of internal channels and surface roughness on the high-cycle fatigue performance of Ti-6Al-4V processed by SLM. *Materials & Design* **143**, 1-11 (2018).
135. Froes, F. H. et al. The technologies of titanium powder metallurgy. *JOM* **56**, 46-48 (2004).
136. Soyama, H. & Takeo, F. Effect of various peening methods on the fatigue properties of Titanium alloy Ti6Al4V manufactured by direct metal laser sintering and electron beam melting. *Materials* **13**, 2216 (2020).
137. Hasib, M. T. et al. Fatigue crack growth behavior of laser powder bed fusion additive manufactured Ti-6Al-4V: Roles of post heat treatment and build orientation. *International Journal of Fatigue* **142**, 105955 (2021).
138. Kumar, P. & Ramamurty, U. Microstructural optimization through heat treatment for enhancing the fracture toughness and fatigue crack growth resistance of selective laser melted Ti-6Al-4V alloy. *Acta Materialia* **169**, 45-59 (2019).
139. Cain, V. et al. Crack propagation and fracture toughness of Ti6Al4V alloy produced by selective laser melting. *Additive Manufacturing* **5**, 68-76 (2015).
140. Kumar, P., Prakash, O. & Ramamurty, U. Micro-and meso-structures and their influence on mechanical properties of selectively laser melted Ti-6Al-4V. *Acta Materialia* **154**, 246-260 (2018).
141. Viespoli, L. M. et al. Creep and high temperature fatigue performance of as build selective laser melted Ti-based 6Al-4V titanium alloy. *Engineering Failure Analysis* **111**, 104477 (2020).
142. Kim, Y. K. et al. Improvement in the high-temperature creep properties via heat treatment of Ti-6Al-4V alloy manufactured by selective laser melting. *Materials Science and Engineering: A* **715**, 33-40 (2018).
143. Barboza, M. J. R. et al. Creep behavior of Ti–6Al–4V and a comparison with titanium matrix composites. *Materials Science and Engineering: A* **428**, 319-326 (2006).
144. Lee, D. G. et al. Effects of microstructural factors on quasi-static and dynamic deformation behaviors of Ti-6Al-4V alloys with widmanstätten structures. *Metallurgical and Materials Transactions A* **34**, 2541 (2003).
145. Bertolini, R. et al. Improving surface integrity and corrosion resistance of additive manufactured Ti6Al4V alloy by cryogenic machining. *The International Journal of Advanced Manufacturing Technology* **104**, 2839-2850 (2019).
146. Zhang, Y. F. et al. Electrochemical polishing of additively manufactured Ti–6Al–4V alloy. *Metals and Materials International* **26**, 783-792 (2020).
147. Yang, J. J. et al. Corrosion behavior of additive manufactured Ti-6Al-4V Alloy in NaCl solution. *Metallurgical and Materials Transactions A* **48**, 3583-3593 (2017).
148. Dai, N. W. et al. Corrosion behavior of selective laser melted Ti-6Al-4V alloy in NaCl solution. *Corrosion Science* **102**, 484-489 (2016).
149. Wu, B. T. et al. The anisotropic corrosion behaviour of wire arc additive manufactured Ti-6Al-4V alloy in 3.5% NaCl solution. *Corrosion Science* **137**, 176-183 (2018).
150. Dai, N. W. et al. Distinction in corrosion resistance of selective laser melted Ti-6Al-4V alloy on different planes. *Corrosion Science* **111**, 703-710 (2016).
151. Dai, N. W. et al. Heat treatment degrading the corrosion resistance of selective laser melted Ti-6Al-4V alloy. *Journal of The Electrochemical Society* **164**, C428-C434 (2017).
152. Xu, Y. Z. et al. Effect of annealing treatments on the microstructure, mechanical properties and corrosion behavior of direct metal laser sintered Ti-6Al-4V. *Journal of Materials Engineering and Performance* **26**, 2572-2582 (2017).